RESEARCH ARTICLE

physica status solidi b
www.pss-b.com

First-Principles Investigations of the Structural Phases of Low-Spin State of $BiCoO_3$

Salima Boutiche, Xu He, Hania Djani, and Eric Bousquet*

Herein, from first-principles calculations, the phase diagram of the low-spin (LS) state of $BiCoO_3$ is scrutinized. The phonon-dispersion curves of the cubic phase are analyzed to identify all the possible unstable modes and assessed the energy gain of the resulted distorted phases. In the findings, the presence of similar phases is revealed in both LS and high-spin (HS) states, including ferroelectric and octahedra rotations distortions. However, the relative energy ordering of these phases differs significantly between the two states. Notably, the energy gain from mode condensation is considerably less pronounced in the LS case compared to HS state. Furthermore, it is identified that the common *Pnma* phase is the ground state of the LS state of $BiCoC_3$, closely followed by the *Imma* octahedra rotation phase and the *R3c* ferroelectric phase, hence, different from the *P4mm* ferroelectric ground state of the HS state.

1. Introduction

Bi-based perovskite oxides family topic is a major area of interest within the field of ferroelectricity and multiferroicity.[1,2] Within this family, $BiCoO_3$ stands out for its unique properties. It crystallizes below 733 K in the supertetragonal *P4mm* phase[3] and has a Néel temperature of 470 K[4] such that it is considered as a room-temperature multiferroic. The occurrence of the supertetragonality is manifested by a pronounced ratio of c/a cell parameters of 1.265.[4–6] This elongation, that enables a spontaneous polarization up to 120 μC cm^{-2},[1] is accompanied by a significant displacement of Co^{3+} ions from the central position of the octahedron, such that coordination pattern of Co ions with the adjacent O anions can be seen more like a pyramidal arrangement than the conventional octahedral geometry (see **Figure 1**). The origin of this huge polar displacement is attributed to the interplay between the Co($3d$) and O($2p$) orbitals, leading to a covalent interaction,[6] as well as the inherent spin state of the Co ion.[4,6,7] The Co^{3+} ion displays an electronic configuration of $3d^6$, enabling the adoption of either a high-spin (HS) state (d^6;t2g $(\uparrow)^3$, e.g., $(\uparrow)^2$ t2g $(\downarrow)^1$ that corresponds to the magnetic moment $S = 2$, or a low-spin (LS) state (d^6;t2g $(\uparrow)^3$, e.g., t2g $(\downarrow)^3$) that corresponds to $S = 0$.[8] Multiple investigations have demonstrated the *P4mm* tetragonal ferroelectric ground state of $BiCoO_3$ with C-type antiferromagnetic (C-AFM) ordering and Co^{3+} ions in the HS state.[4,9,10]

Although the C-AFM *P4mm* state is the ground state at low temperature, the LS state can appear upon structural distortions. For example, in the high-symmetry cubic phase, the HS state cannot be stabilized. The crossover from HS to LS state can be enabled with the structural modification by an external field like temperature or external pressure. Notably, the intermediate state in the path of the reversing of the ferroelectric polarization might be LS state.[8] Therefore, the exploration of the phase diagram of the LS is of importance.

Bi-based perovskite oxides exhibit a rich variety of structural instabilities in the cubic phase. These instabilities include ferroelectric and antiferroelectric displacements of cations, rotations of oxygen octahedra, orbital ordering, Jahn–Teller distortions, and charge ordering accompanied by breathing of the oxygen octahedra. These instabilities give rise to a multitude of possible structural phases.[2,9,10] However, although first-principle calculations have shown numerous instabilities in $BiCoO_3$, experimental observations often reveal a single phase transition, from the cubic phase to the supertetragonal *P4mm* phase.[8,10–12]

In this article, we utilize density-functional theory (DFT) calculations to investigate the phonon instabilities and their corresponding phase diagram in the previously unexplored cubic LS phase of $BiCoO_3$. The organization of the article is as follows: we first present the calculated phonon-dispersion curves for the LS state of Co atoms in the cubic phase of $BiCoO_3$. Subsequently, we identify and analyze the unstable phonon modes. We construct the LS phase diagram and compare it to the phase diagram for the HS state.

S. Boutiche
Laboratoire de Chimie Théorique Computationnelle et Photonique
Faculté de chimie
USTHB
B.P.32 El Alia, Bab Ezzouar, 16111 Alger, Algeria

X. He, E. Bousquet
Physique Théorique des Matériaux
Q-MAT
CESAM
Université de Liége
Allée 6 août, 19, B-4000 Sart Tilman, Belgium

H. Djani
Ionized medias and Lasers
Centre de Développement des Technologies Avancées
Cité 20 août 1956, Baba Hassen, 16081 Alger, Algeria
E-mail: hdjani@cdta.dz

The ORCID identification number(s) for the author(s) of this article can be found under https://doi.org/10.1002/pssb.202400131.

DOI: 10.1002/pssb.202400131

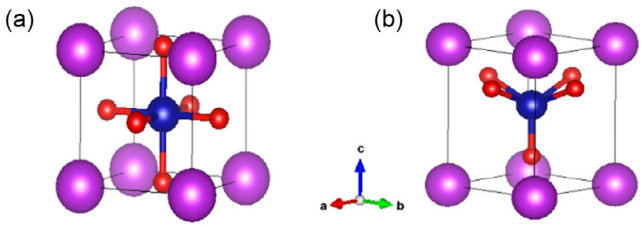

Figure 1. a) Schematic view of the cubic $Pm\bar{3}m$ phase and b) the super-tetragonal $P4mm$ phase of $BiCoO_3$. Purple, blue, and red balls correspond to Bi, Co, and O atoms, respectively.

2. Technical Details

The DFT calculations were performed with the ABINIT code[13,14] and through its projector-augmented-wave (PAW) method[15] implementation. We used the generalized gradient approximation of the Perdew–Becke–Erzenhof[16,17] for the exchange correlation functional due to its successful prediction of the $P4mm$ phase as the ground state.[10] The Liechtenstein flavor of the DFT + U approximation[18] was used for the Co d orbitals with an on-site Coulomb interaction $U = 6$ eV and an on-site exchange interaction $J = 0.2$ eV in the HS case, while, as there is no magnetism and no partially filled orbitals in the LS phase, no U correction was necessary (kept however in the LS calculations to adopt the same computational framework and ensure a fair comparison). Our calculations reveal that the combination of U and J values used in this study gives results nearly identical to those obtained with $U = 6$ eV and $J = 0$ eV in ref. [10]. However, utilizing $J = 0.2$ eV in our calculations led to improved numerical convergence for the HS case.

The atomic data for Bi, Co, and O were taken from the JTH PAW table (v1.0)[19] with Co(3p, 3d and 4s), Bi(5d, 6s and 6p), and O(2s and 2p) treated as valence electrons. We performed integration within the Brillouin zone by using k-point grids of a $6 \times 6 \times 6$ for $Pm\bar{3}m$, $R\bar{3}c$, $R3c$, $R3m$, $I4/mcm$, $6 \times 6 \times 8$ for $P4mm$ (C-AFM), and $6 \times 6 \times 4$ for $Pnma$. The atomic positions were relaxed until a residual stress less than 10^{-5} Ha Bohr^{-3} was reached. The phonon frequencies were calculated within the density-functional perturbation theory,[20] with a q-point mesh of $2 \times 2 \times 2$. The ISOTROPY software[21] was used for symmetry analyses, and VESTA software[22] was used for the visualization of the different structures.

From the phonon band structure, we identified phonon instabilities. We condensed them (single or combined) into the cubic phase to lower the symmetry and then we fully relaxed the distorted structures, that were subsequently analyzed with ISODISTORT from ISOTROPY software[21] to identify the symmetry-adapted mode (SAM) amplitudes.

3. Phonon Dispersion and Instabilities of the Cubic Phase

Our investigation begins with the high-symmetry cubic phase ($Pm\bar{3}m$) of $BiCoO_3$, as depicted in Figure 1a. According to our DFT calculations, this phase is only stable in the nonmagnetic LS state. We employ this LS cubic phase as the reference energy level for our calculations. The relaxed lattice parameter of the cubic cell was determined to be $a = 3.806$ Å.

Calculated phonon-dispersion curves of the LS cubic phase is given in **Figure 2**, negative frequencies in the graph correspond to imaginary phonon frequencies (unstable phonon modes). One can see two types of unstable dispersion branches: i) one with the lowest frequency, which propagates between all high-symmetry points and split at M and R points and involving the motion of all the atoms, but dominated by O motions and Bi atoms; and 2) one that is localized around the M and the R points but strongly disperses away from them and dominated by Bi motions. In **Table 1**, we reported the mode labels and frequencies of the different unstable phonon modes at high-symmetry points of the Brillouin zone and in **Figure 3** we represent the main motions of atoms for each mode.

We can see that the strongest instabilities are associated with in-phase (M_2^+) and out-of-phase (R_5^-) octahedral rotations. This observation aligns with previous HS calculations[10] that reported the presence of numerous phases involving octahedral rotations. Our calculations also showed that antipolar modes are also unstable at all zone boundary points: X_5^- (antipolar motion of Bi and O within the same atomic plane), M_5^- (antipolar motion of Bi in one direction and of Co and O in the perpendicular direction), M_3^- (antipolar motion of the Bi atoms only), and R_4^- (antipolar motion of Bi in one direction and O atoms in the perpendicular directions).

These observations contrast with the behavior observed in the polar unstable branch of, e.g., cubic $BaTiO_3$, where the band show a strong dispersion when approaching the R point.[23] However, it is important to note that this difference arises from

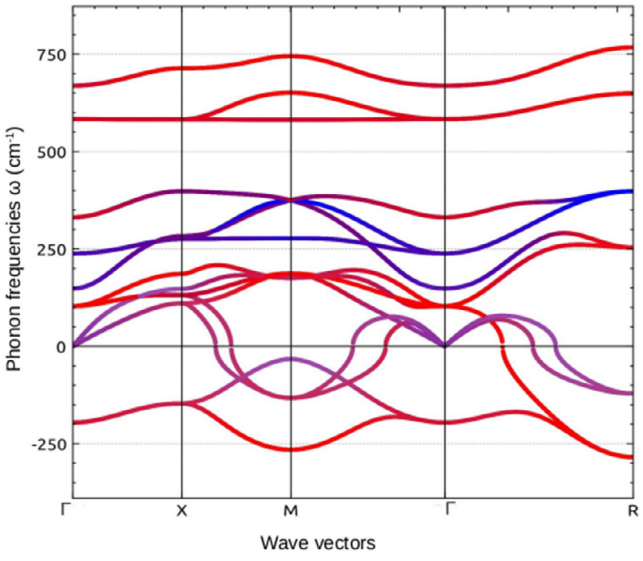

Figure 2. Calculated phonon-dispersion curves of the cubic phase of $BiCoO_3$ along the Γ–X–M–Γ–R path of the Brillouin zone. Imaginary frequencies are plotted with negative numbers. The high-symmetry points coordinates are $\Gamma = (0, 0, 0)$, $X = (1/2, 0, 0)$, $M = (1/2, 1/2, 1/2)$, and $R = (1/2, 1/2, 1/2)$. The dispersion line color has been assigned to each point according to the contribution of each kind of atom to the associated eigenvector and as follows: red for O atoms, purple for Bi atoms, and blue for Co atoms.

Table 1. Modes labels and frequencies (ω, cm^{-1}) of unstable phonon modes at Γ, *X*, *M*, and *R* points of the Brillouin zone of the LS cubic phase of $BiCoO_3$. The third column shows the low-symmetry subgroups that can be reached by condensing the mode eigenvector into the cubic phase (and along one, two, or three directions depending on the degeneracy). The last column gives the gain of energy ΔE (meV $f.u.^{-1}$) with respect to the LS cubic phase, of the fully relaxed phases obtained after condensation of the unstable phonon modes.

Label	ω	Subgroups	ΔE
Γ_4^-	196*i*	*P4mm*	−312
		Amm2	−369
		R3m	−368
X_5^-	147*i*	*Pmma*	−153
		Cmcm	−140
M_2^+	265*i*	*P4/mbm*	−304
M_5^-	133*i*	*CmCm*	−61
		Pmma	−44
M_3^-	33*i*	*P4/nmm*	−16
R_5^-	284*i*	*I4/mcm*	−366
		Imma	−580
		$R\bar{3}c$	−470
R_4^-	121*i*	*I4/mmm*	−167
		Imma	−499
		$R\bar{3}m$	−100

the distinct nature of the unstable modes involved. $BaTiO_3$ has the X_5^+ and M_3^+ modes, while our calculations for $BiCoO_3$ identify the M_2^+ and R_5^- modes as being the unstable modes along the polar branch. Hence, $BiCoO_3$ reveals a distinct profile of unstable phonon modes compared to other perovskite oxides like $BaTiO_3$ and $PbTiO_3$. While both $PbTiO_3$ and $BaTiO_3$ share the same unstable mode labels X_5^+ and M_3^+, only $PbTiO_3$ exhibits additional instabilities seen in $BiCoO_3$, namely the X_5^- antipolar mode, M_2^+ in-phase rotation, and R_5^- out-of-phase rotation. Notably, the M_3^-, M_5^-, and R_4^- unstable modes observed in $BiCoO_3$ are absent in both $BaTiO_3$ and $PbTiO_3$. Furthermore, the unstable phonon frequencies in $BiCoO_3$ are stronger than those observed in other ferroelectric perovskites, for example, $150i\,cm^{-1}$ reported for $PbTiO_3$[24] versus $200i\,cm^{-1}$ in the LS phase of $BiCoO_3$.

4. Condensation of Unstable Modes and Phase Diagram of LS $BiCoO_3$

After the identification of the primary unstable instabilities, we condensed their related eigenvectors into the cubic LS phase of $BiCoO_3$ to reach the lower energy phases. In Table 1, we report the space groups of the low-symmetry phases after the condensation of single unstable phonon modes. The polar unstable mode Γ_4^- can give three polar phases when condensed along one, two, or three directions, *P4mm*, *Amm2*, and *R3m*, respectively, as usually found in the ferroelectric perovskite oxides[25–27] The out-of-phase octahedra rotation R_5^- unstable mode gives the *I4/mcm*, *Imma*, and $R\bar{3}c$ space groups (corresponding to the Glazer notation $a^0a^0c^-$, $a^-a^-b^0$, and $a^-a^-a^-$, respectively). These phases have been observed in various perovskites, including $SrTiO_3$ (*I4/mcm*)[28] and $LaAlO_3$ ($R\bar{3}c$).[29] The freezing of the nondegenerate M_2^+ in-phase octahedra rotations results in the *P4/mbm* space groups with the Glazer's notation $a^0a^0c^+$. The antipolar mode M_3^- gives the *P4/nmm* space group that corresponds to the high-temperature antiferroelectric phase observed in WO_3.[30,31] The other unstable modes, M_5^- and X_5^- are antipolar modes that are usually stable in most perovskites but are often at play as secondary distortions coupled to the aforementioned distortions, like in the most common *Pnma* ground-state phase of perovskites (combination of two directions of R_5^- and one direction of M_2^+ unstable modes, i.e., $a^-a^-c^+$ octahedra rotations, giving rise to the appearance of the secondary X_5^- distortion through improper coupling).[32]

The last column of Table 1 presents the energy gain associated with the condensation of each phonon mode in one, two, or three directions, depending on its degeneracy. Notably, the R_5^- out-of-plane octahedra rotation mode exhibits the largest energy gain (-580 meV $f.u.^{-1}$) when condensed along two directions, leading to the *Imma* phase. This observation deviates from the typical behavior in perovskite oxides, where the $R\bar{3}c$ phase resulting from the condensation of the R_5^- mode along the three directions is the one generally favored.[32] This gain of energy is followed by the antipolar R_4^- mode that also exhibits a large energy gain of -499 meV $f.u.^{-1}$ when condensed along two directions, resulting also in an *Imma* phase but with different Wyckoff positions. Notably, the observation of this antipolar displacement as an unstable mode with such a significant energy gain in $BiCoO_3$ differs from typical perovskite oxides, where such behavior has not been reported. Interestingly, we obtain that in contrast to the HS state of $BiCoO_3$, the polar distortions do not give the largest gain of energy in the LS state of $BiCoO_3$. Hence, we can conclude that the Bi lone pair is not enough to explain the stabilization of the supertetragonal ferroelectric *P4mm* ground state found in the HS state of $BiCoO_3$ and that the Co d-orbital occupations are at play to stabilize this ground-state phase as reported in the literature.[6,7,33]

From **Figure 4**, we can see that in the LS state, the condensation of individual unstable modes is not sufficient to reach the lowest energy ground state. For that the combination of different unstable modes is necessary. As a matter of fact, combining the polar Γ_4^- and the out-of-phase octahedra rotation R_5^- modes in the three directions gives the *R3c* phase. Interestingly, the *Pnma* phase, characterized by Glazer notation $a^-b^+c^-$, emerges as the ground state for the LS state of $BiCoO_3$. The *Pnma* phase includes the in-phase M_2^+ rotation in one direction and the out-of-phase R_5^- rotation in two directions, in addition to a small contribution from secondary modes like X_5^-, R_4^-, and the Jahn–Teller distortion. These extra modes are coming from trilinearly couplings with the with M_2^+ and the R_5^- modes, as reported by Benedek et al.[32] The presence of the Jahn–Teller distortion in the *Pnma* phase is not surprising as the Jahn–Teller distortion

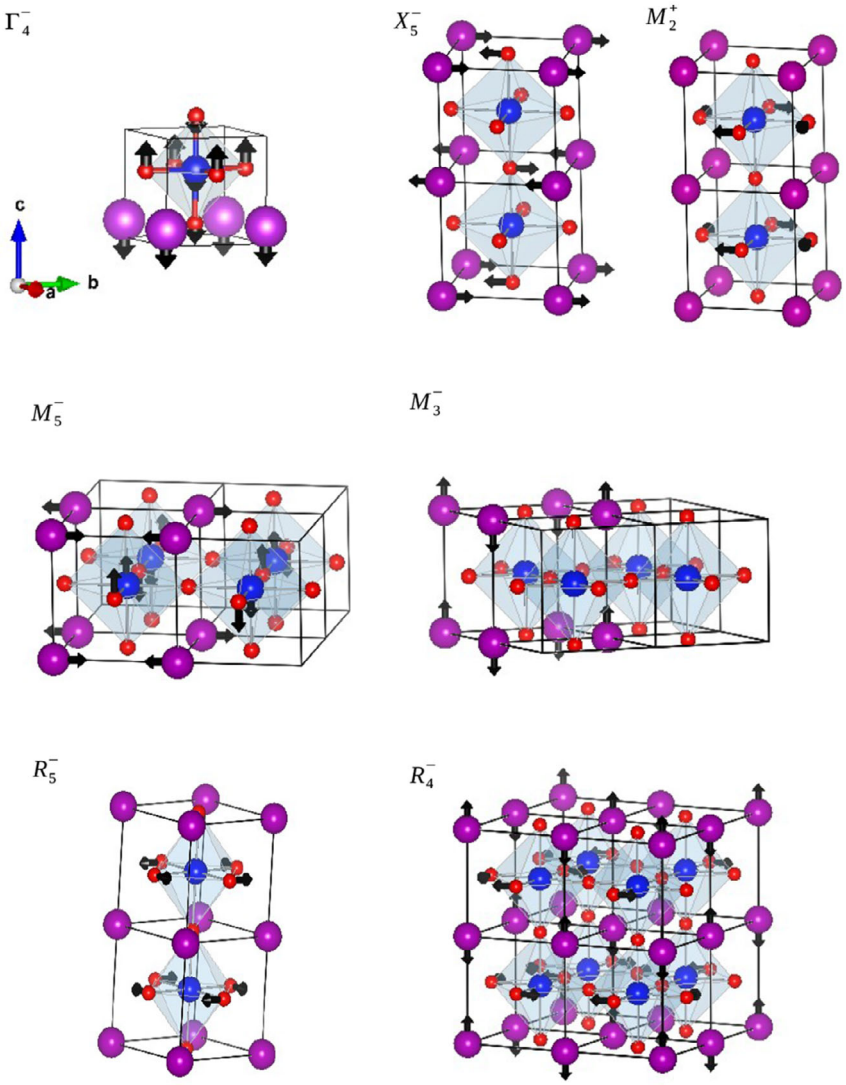

Figure 3. Schematic view of the unstable phonon modes eigendisplacements of the low-spin cubic phase of $BiCoO_3$ (O atoms in red, Co atoms in blue, and Bi atoms in purple): Γ_4^- (polar distortion), M_2^+ (in-phase octahedra rotation), R_5^- (out-of-phase octahedra rotation), X_5^- (antipolar motion of Bi and O within the same atomic plane), M_5^- (antipolar motion of Bi in one direction and of Co and O in perpendicular direction), M_3^- (antipolar motion of the Bi atoms only), and R_4^- (antipolar motion of Bi and O atoms but in different directions). Only one direction of degenerate modes is shown for clarity.

is always allowed into the *Pnma* perovskite phase,[34] even if, as here, the cation is not Jahn–Teller active. However, the observed distortion in $BiCoO_3$ might be more pronounced compared to other non-Jahn–Teller *Pnma* phases and exhibits sensitivity to strain as reported for $CaMnO_3$.[35–37]

Surprisingly, we found that the *Imma* phase, with only two out-of-phase octahedra rotations ($a^0a^-a^-$) is only 1 meV f.u.$^{-1}$ higher than the *Pnma* structure, such that these two phases are quasi degenerate. Our calculations for the LS state of $BiCoO_3$ predict that the most stable polar phase is the *R*3*c* phase, similar to the ground state of $BiFeO_3$.[38,39] This *R*3*c* polar phase is energetically close to the *Pnma* ground state, with an energy difference of 15 meV f.u.$^{-1}$ only. This suggests that the polar phase could be further stabilized experimentally through, e.g., strain engineering techniques.[40,41] However, it is important to note that, despite the larger ionic radii of HS Co^{3+} (0.75 Å) compared to LS Co^{3+} (0.69 Å), both the LS and HS states of $BiCoO_3$ are expected to exhibit a tendency toward a nonpolar antiferrodistortive phase due to their tolerance factors being lower than 1.[32] Comparing the LS and HS phases in Figure 4 reveals significantly larger energy gains for the HS case. Notably, the HS ground state exhibits the *P*4*mm* phase with a single polar distortion, Γ_4^-, characterized by a significant displacement amplitude of 1.34 Å. This amplitude is substantially larger compared to the 0.89 Å observed for the LS *P*4*mm* phase (**Table 2**). These findings suggest that the HS electronic state of

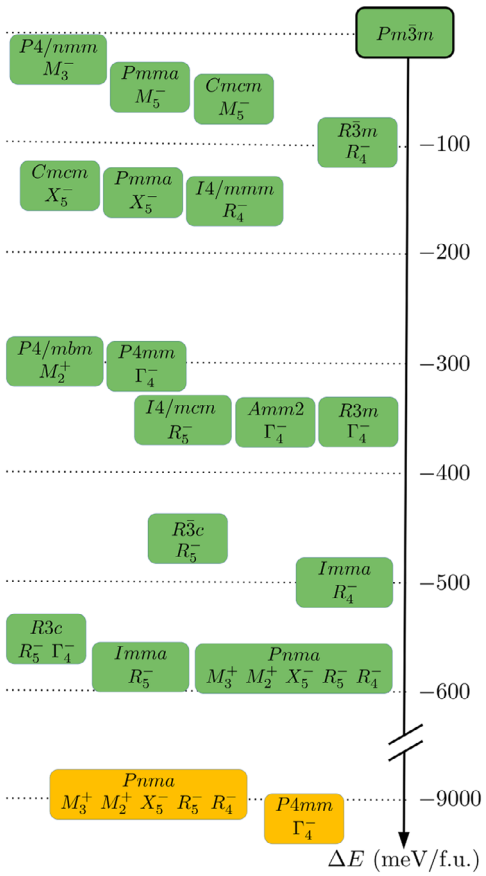

Figure 4. Schematic phase diagram of the gain of energy (meV f.u.$^{-1}$) of the LS case of $BiCoO_3$ (green color) and the two lowest energy phases of the HS case in its C-AFM magnetic phase (yellow color). In each case, we give the space group and the SAM mode labels that contribute to the distortion. The LS $Pm\bar{3}m$ cubic phase is taken as the zero energy reference for both HS and LS. Only the two lowest energy phases of the HS case are shown for clarity.

Co significantly enhances the polar distortion, potentially due to the energy gain achieved by lifting the degeneracy of the d_{xy} and the d_{yz}/d_{xz} orbitals through the tetragonality introduced by the distortion. This difference may be the reason why the polar *P4mm* phase is not among the lowest energy LS states.[6]

Interestingly, the second lowest energy state in the HS phase adopts a *Pnma* structure and exhibits a combination of unstable phonon modes like R_5^- (with an SAM amplitude of 2.89 Å), M_2^+ (2.50 Å), R_4^- (0.33 Å), X_5^- (1.59 Å), and M_3^+ (0.08 Å). Notably, all the corresponding SAM amplitudes in the HS *Pnma* phase are significantly larger compared to their counterparts in the LS phase. This observation reiterates the trend of enhanced distortion amplitudes in the HS state.

Hence, since our calculations predict the *Pnma* phase as the most stable configuration for the LS state of $BiCoO_3$, it would suggest that a hypothetical transition from the HS to LS state would involve a more intricate transformation beyond a straightforward conversion from the HS *P4mm* phase to its LS counterpart.

Table 2. Symmetry-adapted mode (SAM) amplitudes as calculated with the ISODISTORT from ISOTROPY software (in Å) for each distorted LS structure after a full relaxation. We report the imaginary frequency of the corresponding unstable mode when present (in brackets, in cm^{-1}).

Phase	Γ_4^-	X_5^-	M_2^+	M_5^-	M_3^-	R_5^-	R_4^-	M_3^+
LS	[196*i*]	[147*i*]	[265*i*]	[133*i*]	[33*i*]	[284*i*]	[121*i*]	JT
P4mm	0.89	–	–	–	–	–	–	–
Amm2	0.84	–	–	–	–	–	–	–
R3m	0.86	–	–	–	–	–	–	–
Pmma	–	0.53	–	–	–	–	–	–
Cmcm	–	0.53	–	–	–	–	–	–
P4/mbm	–	–	0.83	–	–	–	–	–
Cmcm	–	–	–	0.38	–	–	–	–
Pmma	–	–	–	0.32	–	–	–	–
P4/nmm	–	–	–	–	0.41	–	–	–
I4/mcm	–	–	–	–	–	0.79	–	–
Imma	–	–	–	–	–	1.38	–	–
R3̄c	–	–	–	–	–	0.96	–	–
I4/mmm	–	–	–	–	–	–	0.51	–
Imma	–	–	–	–	–	–	0.92	–
R3̄m	–	–	–	–	–	–	0.60	–
R3c	1.08	–	–	–	–	0.86	–	–
Pnma	–	1.11	1.75	–	–	2.24	0.16	0.05

5. Conclusion

In this work, we used DFT calculations to build the structural phase diagram of the nonmagnetic, LS state of $BiCoO_3$. Our analysis of the phonon-dispersion curves for the cubic phase revealed numerous phonon instabilities, including both commonly observed modes in cubic perovskites (e.g., polar instability, octahedral rotations) and less frequently reported ones (e.g., antipolar modes M_3^-, M_5^-, and R_4^-).

Condensation of these various phonon modes led to the *Pnma* phase to be the lowest energy configuration for the LS state, i.e., the most common ground state observed in perovskites. Notably, we also obtained that the *Imma* phase follows closely the *Pnma* in terms of energy, resulting in a quasi-degenerate state. This finding is surprising as the *Pnma* phase includes an additional in-phase octahedral rotation compared to the *Imma* phase, leading to several secondary distortions through improper-like coupling. While the condensation of the polar modes leads to an energy gain in the LS case, their overall energy remains significantly higher compared to the ground state. Conversely, the *P4mm* ferroelectric phase emerges as the ground state in the HS phase, followed by the *Pnma* phase. These observations reinforce the critical role of Co^{3+} orbital filling in stabilizing the supertetragonal ferroelectric phase. This study opens the way for future investigations exploring the experimental stabilization of the LS phase within a pressure or strain phase diagram. Furthermore, the contrasting phase diagrams of the LS and HS states support previous conclusions highlighting the crucial role of Co in stabilizing the HS state.[7,33]

Acknowledgements

The authors would like to thank Erasmus+ international Credit Mobility program (2016–2018 édition). The computational resources have been provided by the Consortium des Équipements de Calcul Intensif (CÉCI), funded by the Fonds de la Recherche Scientifique (F.R.S.-FNRS) under grant no. 2.5020.11, and the Tier-1 Lucia supercomputer of the Walloon Region, infrastructure funded by the Walloon Region under the grant agreement no. 1910247 and the CDTA cloud platform.

Conflict of Interest

The authors declare no conflict of interest.

Data Availability Statement

The data that support the findings of this study are available from the corresponding author upon reasonable request.

Keywords

density-functional theory (DFT) calculations, multiferroics, perovskites

Received: March 12, 2024
Revised: May 8, 2024
Published online: May 24, 2024

[1] M. Guennou, M. Viret, J. Kreisel, *C. R. Phys.* **2015**, *16*, 182.
[2] A. A. Belik, *J. Solid State Chem.* **2012**, *195*, 32.
[3] K. Oka, M. Azuma, W.-T. Chen, H. Yusa, A. A. Belik, E. Takayama-Muromachi, M. Mizumaki, N. Ishimatsu, N. Hiraoka, M. Tsujimoto, M. Tsujimoto, M. G. Tucker, J. P. Attfield, Y. Shimakawa, *J. Am. Chem. Soc.* **2010**, *132*, 9438.
[4] A. A. Belik, S. Iikubo, K. Kodama, N. Igawa, S.-I. Shamoto, S. Niitaka, M. Azuma, Y. Shimakawa, M. Takano, F. Izumi, E. Takayama-Muromachi, *Chem. Mater.* **2006**, *18*, 798.
[5] N. Cohen, O. Diéguez, *Isr. J. Chem.* **2020**, *60*, 833.
[6] Y. Okuno, Y. Sakashita, *Jpn. J. Appl. Phys.* **2010**, *49*, 09ME08.
[7] H. Ishizaki, H. Yamamoto, T. Nishikubo, Y. Sakai, S. Kawaguchi, K. Yokoyama, Y. Okimoto, S.-Y. Koshihara, T. Yamamoto, M. Azuma, *Inorg. Chem.* **2019**, *58*, 16059.
[8] L. Weston, X. Y. Cui, S. P. Ringer, C. Stampfl, *Phys. Rev. B* **2016**, *93*, 165210.
[9] A. Singh, V. N. Singh, E. Canadell, J. Íñiguez, O. Diéguez, *Phys. Rev. Mater.* **2018**, *2*, 104417.
[10] C. Cazorla, O. Diéguez, J. Íñiguez, *Sci. Adv.* **2017**, *3*.
[11] X. Ming, X. Meng, F. Hu, C.-Z. Wang, Z.-F. Huang, H.-G. Fan, G. Chen, *J. Phys.: Condens. Matter* **2009**, *21*, 295902.
[12] M. Azuma, S. Niitaka, N. Hayashi, K. Oka, M. Takano, H. Funakubo, Y. Shimakawa, *Jpn. J. Appl. Phys.* **2008**, *47*, 7579.
[13] X. Gonze, F. Jollet, F. Abreu Araujo, D. Adams, B. Amadon, T. Applencourt, C. Audouze, J.-M. Beuken, J. Bieder, A. Bokhanchuk, E. Bousquet, F. Bruneval, D. Caliste, M. Côté, F. Dahm, F. Da Pieve, M. Delaveau, M. Di Gennaro, B. Dorado, C. Espejo, G. Geneste, L. Genovese, A. Gerossier, M. Giantomassi, Y. Gillet, D. R. Hamann, L. He, G. Jomard, J. Laflamme Janssen, S. Le Roux, et al., *Comput. Phys. Commun.* **2016**, *205*, 106.
[14] X. Gonze, B. Amadon, G. Antonius, F. Arnardi, L. Baguet, J.-M. Beuken, J. Bieder, F. Bottin, J. Bouchet, E. Bousquet, N. Brouwer, F. Bruneval, G. Brunin, T. Cavignac, J.-B. Charraud, W. Chen, M. Côté, S. Cottenier, J. Denier, G. Geneste, P. Ghosez, M. Giantomassi, Y. Gillet, O. Gingras, D. R. Hamann, G. Hautier, X. He, N. Helbig, N. Holzwarth, Y. Jia, et al., *Comput. Phys. Commun.* **2020**, *248*, 107042.
[15] P. E. Blöchl, *Phys. Rev. B* **1994**, *50*, 17953.
[16] C. Loschen, J. Carrasco, K. M. Neyman, F. Illas, *Phys. Rev. B* **2007**, *75*, 035115.
[17] J. P. Perdew, K. Burke, M. Ernzerhof, *Phys. Rev. Lett.* **1998**, *80*, 891.
[18] A. Liechtenstein, V. Anisimov, J. Zaanen, *Phys. Rev. B* **1995**, *52*, 5467.
[19] F. Jollet, M. Torrent, N. Holzwarth, *Comput. Phys. Commun.* **2014**, *185*, 1246.
[20] X. Gonze, C. Lee, *Phys. Rev. B* **1997**, *55*, 10355.
[21] H. T. Stockes, D. M. Hatch, B. J. Campbell, *ISOTROPY* **2007**. https://stokes.byu.edu/isotropy.html
[22] K. Momma, F. Izumi, *J. Appl. Crystallogr.* **2011**, *44*, 1272.
[23] P. S. H. Ghosez, X. Gonze, J. P. Michenaud, *Ferroelectrics* **1998**, *206*, 205.
[24] P. Ghosez, E. Cockayne, U. V. Waghmare, K. M. Rabe, *Phys. Rev. B* **1999**, *60*, 836.
[25] G. Pálinkás, T. Radnai, *Acta Crystallogr. Sect. A* **1976**, *32*, 666.
[26] S. A. Hayward, S. A. T. Redfern, H. J. Stone, M. G. Tucker, K. R. Whittle, W. G. Marshall, *Z. Kristallogr. - Cryst. Mater.* **2005**, *220*, 735.
[27] P. Baranek, *AIP Conf. Proc.* **2007**, *963*, 379.
[28] Y. G. Abreu, J. C. Soares, R. L. Moreira, A. Dias, *J. Phys. Chem. C* **2016**, *120*, 16960.
[29] X. Luo, B. Wang, *J. Appl. Phys.* **2008**, *104*, 073518.
[30] H. Hamdi, E. K. H. Salje, P. Ghosez, E. Bousquet, *Phys. Rev. B* **2016**, *94*, 245124.
[31] H. Hassani, B. Partoens, E. Bousquet, P. Ghosez, *Phys. Rev. B* **2022**, *105*, 014107.
[32] N. A. Benedek, C. J. Fennie, *J. Phys. Chem. C* **2013**, *117*, 13339.
[33] J. Zhao, S.-C. Haw, X. Wang, Z. Hu, C.-Y. Kuo, S.-A. Chen, H. Ishii, N. Hiraoka, H.-J. Lin, C.-T. Chen, Z. Li, A. Tanaka, C.-E. Liu, R. Yu, J.-M. Chen, C. Jin, *Phys. Status Solidi B* **2021**, *258*, 2100117.
[34] M. M. Schmitt, Y. Zhang, A. Mercy, P. Ghosez, *Phys. Rev. B* **2020**, *101*, 214304.
[35] J. Varignon, M. Bibes, A. Zunger, *Phys. Rev. Res.* **2019**, *1*, 033131.
[36] J. Varignon, N. C. Bristowe, E. Bousquet, P. Ghosez, *Sci. Rep.* **2015**, *5*, 15364.
[37] J. Varignon, N. C. Bristowe, P. Ghosez, *Phys. Rev. Lett.* **2016**, *116*, 057602.
[38] P. Ravindran, R. Vidya, A. Kjekshus, H. Fjellvåg, O. Eriksson, *Phys. Rev. B* **2006**, *74*, 224412.
[39] J. B. Neaton, C. Ederer, U. V. Waghmare, N. A. Spaldin, K. M. Rabe, *Phys. Rev. B* **2005**, *71*, 014113.
[40] O. Copie, J. Varignon, H. Rotella, G. Steciuk, P. Boullay, A. Pautrat, A. David, B. Mercey, P. Ghosez, W. Prellier, *Adv. Mater.* **2017**, *29*, 1604112.
[41] H. Tian, S. Cui, L. Fu, H. Zhang, C. Li, Y. Cui, A. Mao, *Nanomaterials* **2023**, *13*, 2342.